Phase diagram for ensembles of random close-packed Ising-like dipoles as a function of texturation

Juan J. Alonso,[1,2,*] B. Allés,[3,†] and V. Russier[4,‡]

[1]*Física Aplicada I, Universidad de Málaga, 29071 Málaga, Spain*

[2]*Instituto Carlos I de Física Teórica y Computacional, Universidad de Málaga, 29071 Málaga, Spain*

[3]*INFN–Sezione di Pisa, Largo Pontecorvo 3, 56127 Pisa, Italy*

[4]*ICMPE, UMR 7182 CNRS and UPE 2-8 rue Henri Dunant 94320 Thiais, France*

(Received 4 August 2019; revised manuscript received 11 September 2019; published 8 October 2019)

We study random close-packed systems of magnetic spheres by Monte Carlo simulations in order to estimate their phase diagram. The uniaxial anisotropy of the spheres makes each of them behave as a single Ising dipole along a fixed easy axis. We explore the phase diagram in terms of the temperature and the degree of alignment (or *texturation*) among the easy axes of all spheres. This degree of alignment ranges from the textured case (all easy axes pointing along a common direction) to the nontextured case (randomly distributed easy axes). In the former case, we find long-range ferromagnetic order at low temperature but, as the degree of alignment is diminished below a certain threshold, the ferromagnetic phase gives way to a spin-glass phase. This spin-glass phase is similar to the one previously found in other dipolar systems with strong frozen disorder. The transition between ferromagnetism and spin glass passes through a narrow intermediate phase with quasi-long-range ferromagnetic order.

DOI: 10.1103/PhysRevB.100.134409

I. INTRODUCTION

The study of ensembles of magnetic nanoparticles (NPs) is an active field of research due to their potential application in areas as disparate as biomedicine, data storage, or nanofluids [1,2]. Current technology allows us to synthesize NPs with a wide variability of sizes and shapes, in addition to coating them with nonmagnetic layers. Moreover, they can be produced in nearly monodisperse ensembles so as to enjoy good control of their spatial distribution [3]. This know-how opens the possibility to realize densely packed ensembles of NPs that behave as systems of interacting dipoles. It is the magnetic order of such structures that stirs a renewed interest in their use in technological applications [4,5].

NPs with diameters d_p up to a few tens of nanometers have a single domain (typical values are 15 nm for Fe, 35 nm for Co, 30 nm for maghemite γ-Fe_2O_3) that behaves as a magnetic dipole [6]. Even when they are spherical, such NPs can have anisotropies that oblige the dipole to lie along a local easy axis and to surmount an anisotropy energy barrier E_a whenever the magnetic moment is inverted, resulting in a blocking temperature $T_b \simeq E_a/30k_B$ [2,4]. When the NPs are closely packed, their dipolar interaction energies E_{dd} are not negligible but typically larger than $E_a/10$, leading to $E_{dd}/k_BT_b \gtrsim 3$. Consequently, low-temperature signatures of collective order induced by the dipolar interaction can be (and have indeed been) observed experimentally [7]. This is to be compared with the super-paramagnetism observed in very diluted systems for which $E_{dd}/k_BT_b \ll 1$ [2,8].

Dilute dispersions of NPs gather into highly ordered three-dimensional (3D) supercrystals on account of their ability to self-assemble after the evaporation of the solvent [9,10]. Such crystals exhibit dipolar super-ferromagnetism in fcc, bcc of I-tetragonal lattices. This behavior was predicted to exist in such lattices by Luttinger and Tisza [11].

Less ordered (noncrystalline) dense packings may be obtained by pressing powders to obtain a granular solid [12], or in concentrated colloidal suspensions by freezing the carrier fluid [13]. The frozen disorder on the positions of the NPs and on the orientation of the anisotropy axes in those systems may induce frustration resulting in super spin-glass (SG) behavior [14,15]. This behavior, originated by dipolar interactions, has been observed experimentally in random close-packed (RCP) samples of dipolar spheres [7] with volume fractions ϕ about 64% [16]. An equilibrium SG phase for nontextured RCP ensembles of dipolar spheres has recently been found by numerical simulations [17].

Nevertheless, the role of positional and orientational disorder in noncrystalline ensembles is far from being completely understood. Numerical simulations have shown that frozen amorphous densely packed systems with volume fractions as high as $\phi = 0.42$ order ferromagnetically provided they are textured [18,19]. This texturation shows up in colloidal suspensions by freezing the solution in the presence of large magnetic fields h [20]. Even when $h = 0$, ensembles of dipolar spheres moving in a nonfrozen fluid with volume fractions as low as 42% tend spontaneously to become textured by aligning their axes, exhibiting nematic order (i.e., with no positional long range order) [21,22].

The picture that emerges is that the ordering of dense noncrystalline systems may change from ferromagnetic (FM) to

*jjalonso@uma.es

†alles@pi.infn.it

‡russier@icmpe.cnrs.fr

SG as the anisotropy-axes alignment dwindles from textured [i.e., parallel axes dipoles (PAD)] to nontextured [random oriented axes dipoles (RAD)].

The purpose of the present work is to depict the phase diagram of noncrystalline dense packings of Ising dipoles with different degrees of texturation by employing Monte Carlo (MC) simulations (see Fig. 2). In this effort, special attention will be paid to (i) examine whether a SG phase exists comparable to the one previously found for very diluted as well as RAD systems of Ising dipoles, and (ii) explore the transition between FM and SG in order to look for possible intermediate phases. We will pursue this investigation on ensembles of Ising dipoles placed at the center of RCP spheres that occupy a 64% fraction of the entire volume. Given that here we do not focus on time-dependent properties, we concede to the Ising dipoles (i.e., dipoles with large anisotropy energies) all the necessary time to flip up and down along their easy axes and reach equilibrium, which is tantamount to saying that we choose $T_b = 0$. Such a model may be relevant for experimental situations in which one expects $E_a \sim 10E_{dd}$ [7]. To investigate the effect of the easy axes alignment, we will introduce a parameter σ that interpolates from the textured to the completely random axes cases. The nature of the low-temperature phases is investigated by measuring the spontaneous magnetization, the SG overlap parameter, and the associated fluctuations and probability distributions.

The paper is organized as follows. In Sec. II we carefully define the model, give the details of the MC algorithm, and introduce the observables that will be measured. The results are presented in Sec. III, and some concluding remarks are given in Sec. IV.

II. MODEL, METHOD, AND OBSERVABLES

A. Model

We study RCP systems of N identical NPs that behave as single magnetic Ising dipoles. The NPs are labeled with $i = 1, \ldots, N$. We will regard each NP as a sphere of diameter d carrying a permanent pointlike magnetic moment $\vec{\mu}_i = \mu s_i \widehat{a}_i$ at its center, where the unit vector $\widehat{a}_i$ is the local easy axis and $s_i = \pm 1$.

The Hamiltonian governing the interaction is

$$\mathcal{H} = \sum_{\langle i,j \rangle} \varepsilon_d \left(\frac{d}{r_{ij}}\right)^3 \left(\widehat{a}_i \cdot \widehat{a}_j - \frac{3(\widehat{a}_i \cdot \vec{r}_{ij})(\widehat{a}_j \cdot \vec{r}_{ij})}{r_{ij}^2}\right) s_i s_j, \quad (1)$$

where $\varepsilon_d = \mu_0 \mu^2/(4\pi d^3)$ is an energy and μ_0 is the magnetic permeability in vacuum. $\vec{r}_{ij}$ is the vector position of dipole j viewed from dipole i, and $r_{ij} = \|\vec{r}_{ij}\|$. The summation runs over all pairs of dipoles i and j, with $i \neq j$. The particles' positions as well as their easy axes $\widehat{a}_i$ remain fixed during the simulations.

The spheres are placed in frozen RCP configurations in a cube of edge L assuming periodic boundary conditions. As in previous work [17], these configurations are obtained by using the Lubachevsky-Stillinger algorithm [23,24], in which the spheres, which are initially very small, are allowed to move and collide while growing in size at a sufficiently high rate until the sample gets eventually stuck in a noncrystalline state with volume fraction $\phi = 0.64$ [16,24]. We shall specify the size of the system by the number N of spheres inside it, or, equivalently, by the lateral size of the cube they fill to capacity,

$$L = \left(\frac{N\pi}{6\phi}\right)^{1/3} d, \quad (2)$$

where d is the final diameter attained by the spheres after they stopped growing.

To investigate the effect of texturation, we consider that the alignment of the vectors $\widehat{a}_i$ with the direction $\widehat{z}$ follows a Gaussian-like distribution,

$$p(\theta_i) \propto \left\{e^{-\theta_i^2/2\sigma^2} + e^{-(\theta_i-\pi)^2/2\sigma^2}\right\} \sin\theta_i, \quad (3)$$

where θ_i is the polar angle of the ith dipole, while each azimuthal angle is chosen at random. The variance σ controls the degree of texturation, intended as the amount of alignment of the easy axes along the Cartesian axis $\widehat{z}$. σ ranges from $\sigma = 0$ for textured systems (PAD) to $\sigma = \infty$ for nontextured samples with axes completely oriented at random (RAD).

We let each Ising dipole flip up and down along its easy axis $\widehat{a}_i$, assuming that the dipoles are able to overcome the local anisotropy barriers. In what follows, distances and temperatures will be given in units of d and ε_d/k_B, respectively, where k_B is Boltzmann's constant.

B. Samples

We define a *sample* $\mathcal{J}$ as a given, arbitrary realization of disorder that, for the systems under study, comes from two sources: from the randomness of the positions of the spheres, and from the degree of texturation or of alignment of their easy axes $\widehat{a}_i$. This disorder does not participate in the dynamics but remains frozen during MC simulations. Only the signs s_i evolve during a simulation.

As a consequence of the above definitions, we shall use the word *configuration* for any set of N signs $\{s_i\}_{i=1,\ldots,N}$. In Figs. 1(a) and 1(b), two statistically independent configurations obtained from a given sample by MC simulation are depicted. Dark blue (red) spheres in the figures denote dipoles pointing up (down) along axes $\widehat{a}_i$ nearly parallel to $\widehat{z}$, while light grayish spheres denote those whose axes deviate significantly from $\widehat{z}$.

Results susceptible to being compared with empirical data require an average over N_s independent samples. The need for this average is crucial at large σ due to the sizable sample-to-sample fluctuations that appear in this regime, where SG order is expected. Moreover, because of the lack of self-averaging associated with SG order, we have not made N_s smaller with increasing N. However, for large systems (the largest ones contain $N = 1728$ dipoles) we could employ no more than 3000 samples because of computer time limitations. The number of samples N_s is listed in Table I for the values of N and σ explored in the simulations.

C. Method

Since by decreasing the degree of texturation the system could end up in a SG phase, we have performed parallel simulations with the tempered Monte Carlo (TMC) algorithm, as this algorithm has proved to be satisfactorily efficient in beating slowing down [25]. Indeed, the TMC method allow

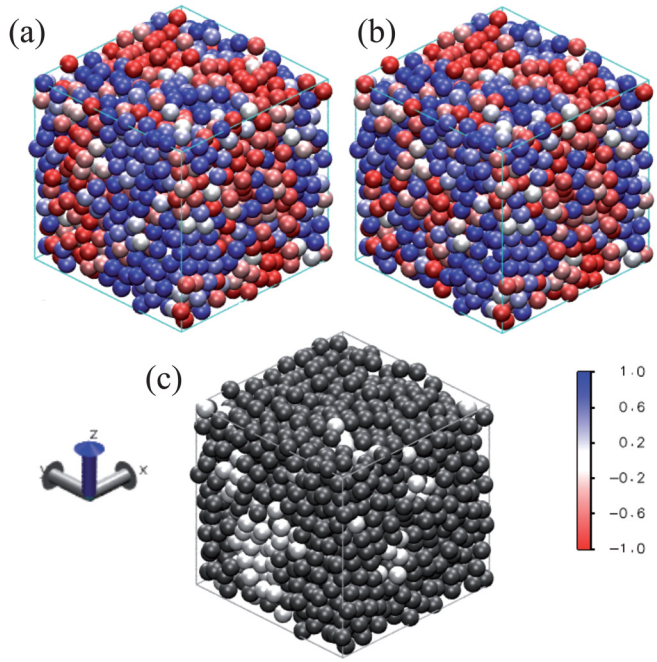

FIG. 1. Parts (a) and (b) show two statistically independent configurations of a sample with 1728 magnetic nanospheres with $\sigma = 0.6$ at the temperature $T = 0.55$. The position of the spheres and the orientation of their local easy axes are both frozen. The color of each sphere i stands for the value of the z component of the magnetic moment $\vec{\mu}_i/\mu = s_i\widehat{a}_i$, where $\widehat{a}_i$ is the local easy axis and $s_i = \pm 1$. Part (c) represents the overlap between the configurations (a) and (b). Black (white) spheres in (c) means $s_i^{(a)}s_i^{(b)} = +1$ (-1).

replicas to overcome energy barriers within which the system could sink and remain confined at low temperatures. These potential wells are minima of the rough energy landscapes that characterize glassy phases. Concretely, for each sample $\mathcal{J}$, we run in parallel $n+1$ identical replicas at temperatures $T = T_{\min} + k\Delta$, where $k = 0, 1, 2, \ldots, n$. We have found it useful to choose the highest temperature, $T_{\max} = T_{\min} + n\Delta$, larger than twice the transition temperature from the paramagnetic (PM) phase to the ordered one. The TMC algorithm involves two steps. In the first one, 10 METROPOLIS sweeps [26] are applied separately to all $n+1$ replicas in order to make them evolve independently from each other. Dipolar fields are updated whenever a sign s_j flip is accepted. After that step, we give to any pair of replicas evolving at neighboring temperatures $(T, T \pm \Delta)$ a chance to be exchanged, according to tempering rules that satisfy detailed balance [25]. We choose Δ such that at least 30% of all attempted exchanges are accepted. Due to limitations in computer time, we simulate systems containing up to $N = 12^3 = 1728$ dipoles and choose $T_{\min}$ larger than half the transition temperature.

We have imposed periodic boundary conditions in the simulations. That means that each dipole i is allowed to interact with all dipoles within an $L \times L \times L$ box centered at i; see (2). Due to the long-range nature of the dipolar-dipolar interaction, we need to take into account contributions from beyond this box by using Ewald's sums [27]. Details on the use of Ewald's sums for dipolar systems are given in Ref. [28]. In these sums, the use of neutralizing Gaussian distributions with standard deviation $\alpha/2$ allows us to split the computation of the dipolar fields into two rapidly convergent sums: a first sum in real space with a cutoff $r_c = L/2$, and a second sum in reciprocal space with a cutoff k_c. We have used $k_c = 10$ and $\alpha = 7.9/L$

TABLE I. The values taken by the parameters utilized in the TMC simulations. σ is the degree of texturation, N is the number of dipoles, N_s is the number of samples with different realizations of disorder, and $T_{\max}$ and $T_{\min}$ are the highest and lowest temperatures, respectively. $\Delta = 0.05$ is the temperature step in all simulations. The number of MC sweeps for equilibration is $t_0 = 10^6$ in all cases. Measurements are taken during the MC sweeps comprised in the interval $[t_0, 2t_0]$.

$\sigma = 0$ ($T_{\max} = 4.5$, $T_{\min} = 1.55$)				
N	216	512	1000	1728
N_s	2100	500	500	500
$\sigma = 0.1$ ($T_{\max} = 4.5$, $T_{\min} = 1.55$)				
N	216	512	1000	
N_s	1000	500	500	
$\sigma = 0.2$ ($T_{\max} = 4$, $T_{\min} = 1.05$)				
N	216	512	1000	
N_s	1000	500	500	
$\sigma = 0.3$ ($T_{\max} = 4$, $T_{\min} = 1.05$)				
N	216	512	1000	1728
N_s	1000	2900	2100	2000
$\sigma = 0.4$ ($T_{\max} = 3.5$, $T_{\min} = 0.55$)				
N	216	512	1000	
N_s	2000	2000	2000	
$\sigma = 0.45$ ($T_{\max} = 3.5$, $T_{\min} = 0.55$)				
N	216	512	1000	1728
N_s	10000	2000	2000	2500
$\sigma = 0.50$ ($T_{\max} = 3.5$, $T_{\min} = 0.55$)				
N	216	512	1000	1728
N_s	10000	8400	6000	2000
$\sigma = 0.53$ ($T_{\max} = 3.5$, $T_{\min} = 0.55$)				
N	216	512	1000	1728
N_s	9800	9600	6500	2000
$\sigma = 0.55$ ($T_{\max} = 3.5$, $T_{\min} = 0.55$)				
N	216	512	1000	1728
N_s	10700	8000	4000	2000
$\sigma = 0.57$ ($T_{\max} = 3.5$, $T_{\min} = 0.55$)				
N	216	512	1000	1728
N_s	11600	10300	5000	3000
$\sigma = 0.60$ ($T_{\max} = 3.5$, $T_{\min} = 0.55$)				
N	216	512	1000	1728
N_s	11000	8000	8400	8200
$\sigma = 0.70, 0.80$ ($T_{\max} = 3.5$, $T_{\min} = 0.55$)				
N	216	512	1000	
N_s	10000	8000	4800	

as a good compromise between accuracy and computational speed [28]. More importantly, given that textured systems in our model are expected to exhibit spontaneous magnetization at low temperatures, we have chosen the so-called conducting external conditions using surrounding permeability $\mu' = \infty$ in order to eliminate shape-dependent depolarizing effects [21,29].

The thermal equilibration times t_0 are assessed by the same procedure of Ref. [17]. The overlap $q(t)$ of configurations created from two replicas of the same sample $\mathcal{J}$ are obtained by evolving the replicas independently after having started from random configurations. Then t_0 is the average over samples of the value of t at which $q(t)$ attains a plateau q_0 for each sample. To test the value thus obtained for t_0, we observed that a second overlap $\widetilde{q}(t_0, t_0 + t)$ calculated for pairs of configurations of a single replica taken at times t_0 and $t_0 + t$ remains stuck to q_0 as t increases [30]. It is found that the less textured the system is, the longer the equilibration time appears. This is due to the large roughness of the free-energy landscapes for nontextured systems. For these hard-to-equilibrate systems, the overlap distributions $p_{\mathcal{J}}(q)$ exhibit numerous spikes associated with the existence of several pure states [31]. In the simulations, we have examined the $\pm q$ symmetry of the overlap distributions $p_{\mathcal{J}}(q)$ as an additional indication that all samples are well thermalized [17].

A double average, the thermal one for each sample $\mathcal{J}$ and the above-mentioned average over the N_s samples, is needed to achieve physical results. The first average is taken within the time interval $[t_0, 2t_0]$. Given an observable u, the result of both averages will be symbolized by $\langle u \rangle$. For simplicity, $\langle |u|^p \rangle$ will often be denoted by u_p. The values of all the simulation parameters are listed in Table I.

D. Observables

The observables that have been measured in the course of the work are the following:

(i) The specific heat c from the fluctuations of the energy $e \equiv \langle \mathcal{H} \rangle / N$.

(ii) The m_z component of the magnetization vector

$$\vec{m} \equiv \frac{1}{N} \sum_i \widehat{a}_i s_i, \tag{4}$$

as a way to characterize the FM behavior. Note that for a given sample, $\vec{m}$ does not rotate during the MC simulation. Rather, it aligns along the nematic director [21,29] $\widehat{\lambda}_{\mathcal{J}}$ that, for the model under study, is the eigenvector corresponding to the largest eigenvalue of the tensor $\mathbb{Q}_{\mathcal{J}} \equiv \frac{1}{2N} \sum_i (3\widehat{a}_i \otimes \widehat{a}_i - \mathbb{I})$. Since $\mathbb{Q}_{\mathcal{J}}$ is constant in time, $\widehat{\lambda}_{\mathcal{J}}$ remains frozen during the simulation.

We find that, for the values of σ considered here, $\widehat{\lambda}_{\mathcal{J}}$ practically coincides with $\widehat{z}$. Then, it makes sense using m_z as the FM order parameter instead of $\|\vec{m}\|$. In fact, we have also computed $\|\vec{m}\|$ and their related quantities and found that they provide the same qualitative results that m_z provides.

(iii) The moments $m_p = \langle |m_z|^p \rangle$ for $p = 1, 2, 4$, that prove useful to calculate the magnetic susceptibility

$$\chi_m \equiv \frac{N}{k_B T} (m_2 - m_1^2), \tag{5}$$

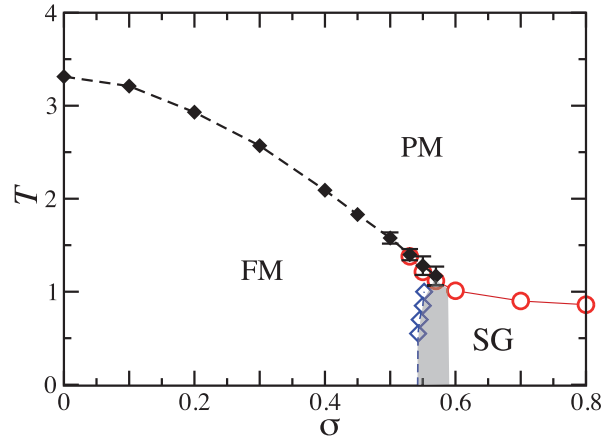

FIG. 2. Phase diagram on the temperature degree of texturation plane for the dipolar Ising model. Symbols ♦ indicate the PM-FM transition, and they have been obtained from the data of B_m vs T. Symbols ○ stand for PM-FM and PM-SG transitions, and they were obtained from the B_q vs T plots. Symbols ◇ represent the FM-SG transition, and they follow from the B_m vs σ plots. The error bars for the data marked with ○ and ◇ are smaller than the size of these symbols. FM quasi-long-range order cannot be discarded in the gray region.

and the dimensionless Binder cumulant

$$B_m \equiv \frac{1}{2} \left(3 - \frac{m_4}{m_2^2} \right). \tag{6}$$

(iv) As a useful tool to look for SG behavior, we calculate the overlap parameter [32],

$$q \equiv \frac{1}{N} \sum_i s_i^{(1)} s_i^{(2)}, \tag{7}$$

given a sample $\mathcal{J}$. $s_j^{(1)}$ and $s_j^{(2)}$ in this expression are the signs at site j of two replicas of the given sample, denoted (1) and (2), that evolve independently in time at the same temperature. Similarly to what has been done for m_z, we also measure $q_p \equiv \langle |q|^p \rangle$ for integer p, and the corresponding Binder parameter $B_q \equiv \frac{1}{2}(3 - \frac{q_4}{q_2^2})$.

(v) Finally, for each sample $\mathcal{J}$ we compute the probability distributions $p_{\mathcal{J}}(m)$ and $p_{\mathcal{J}}(q)$, as well as their average over samples, which will be denoted by $p(m)$ and $p(q)$.

Errors for all quantities are obtained from the mean-squared deviations of the sample-to-sample fluctuations.

III. RESULTS

A. The FM phase

The main result of the paper is the phase diagram on the plane temperature-degree of texturation shown in Fig. 2. It displays regions with FM, PM, and SG phases. The FM order arises at low temperatures in the range $0 \leqslant \sigma \lesssim 0.53$. A thermally driven second-order transition takes place at the phase boundary between the PM and FM phases. Next we give the numerical evidence that supports this interpretation.

FM phases are defined by the presence of a nonvanishing magnetization. In Fig. 3(a) we show the behavior of the moment m_2 with the temperature for $\sigma = 0.3$ in a number of

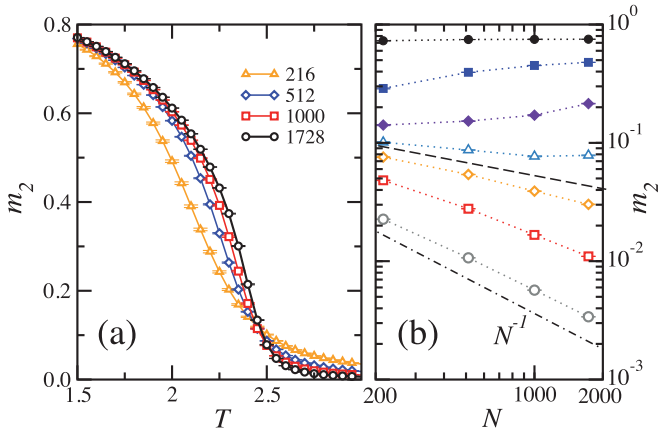

FIG. 3. (a) Plots of the squared magnetization m_2 vs temperature T for $\sigma = 0.3$. △, ◇, □, and ○ stand for $N = 216$, 512, 1000, and 1728 dipoles, respectively. Lines are guides to the eye. (b) Log-log plots of m_2 vs N for different temperatures at $\sigma = 0.3$. From top to bottom: ●, ■, ♦, △, ◇, □, and ○ stand for $T = 1.6$, 2.2, 2.4, 2.5, 2.6, 2.8, and 3.4, respectively. Dotted lines are guides to the eye. The dashed line separates two regimes and stands for a $1/N^{0.35}$ decay. The dot-dashed line shows the N^{-1} decay expected for paramagnets in the thermodynamic limit.

system sizes. We obtain similar results for the magnetization for all values of σ below 0.53. This is evidence of the existence of the FM phase. Figure 4(a) shows plots of the specific heat c versus T. The sharp variation of c near $T = 2.5$ suggests the presence of a singularity as N increases, as is expected for a second-order PM-FM phase transition. The same happens with the plots of the magnetic susceptibility χ_m versus T shown in Fig. 4(b). The data are consistent with a logarithmic divergence of c, and with an approximate power-law divergence of χ_m with N^p (up to logarithmic corrections $\ln N$) where $p \sim 2/3$.

Next we examine the dependence of m_2 on the number N of dipoles. Figure 3(b) shows log-log plots of m_2 versus N for

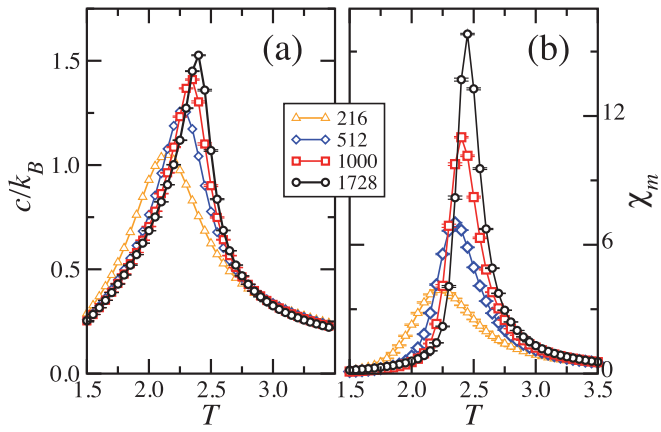

FIG. 4. (a) Plots of the specific heat vs T for $\sigma = 0.3$. △, ◇, □, and ○ stand for systems with $N = 216$, 512, 1000, and 1728 dipoles, respectively. (b) Plots of the magnetic susceptibility χ_m vs T for $\sigma = 0.3$. Same symbols as in (a). Lines in both panels are guides to the eye.

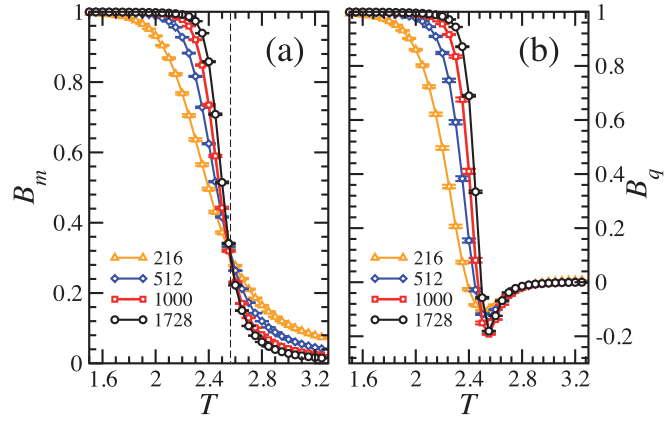

FIG. 5. (a) Plots of the Binder cumulant B_m vs T for $\sigma = 0.3$. △, ◇, □, and ○ stand for systems with $N = 216$, 512, 1000, and 1728 dipoles, respectively. The dashed vertical line indicates the Curie temperature at which the curves cross. (b) Plots of the Binder cumulant for the overlap parameter B_q vs T. Same symbols as in (a). Solid lines in both panels are guides to the eye.

several temperatures. The data at T below $T_c = 2.55(5)$ reflect that m_2 does not vanish in the $N \to \infty$ limit. On the contrary, the plot of m_2 versus N for $T > T_c$ shows a faster than power-law decay with a T-dependent exponent, and consequently the slope of the curves is steeper for increasing T and approaches a $1/N$ trend, which is the expected trend in PM phases. The dashed line in Fig. 3(b) separating the two regimes represents a $1/N^{0.35}$ decay. Although we are aware that these graphs do not allow a precise determination of T_c, we have followed this criterion as a first rough approach for establishing the boundary of the FM phase.

The Binder parameter B_m grants a more precise determination of the transition temperature. It follows from its definition in (6) that $B_m \to 1$ as $N \to \infty$ in the FM phase. On the other hand, from the law of large numbers it follows that, in the PM phase, with short-range FM order, $B_m \to 0$ as N increases. Finally, at a critical point, B_m becomes size-independent, as must occur for every scale-free observable (recall that B_m is dimensionless). The latter is also true in the case of a marginal phase with quasi-long-range magnetic order. Then, curves of B_m versus T for various values of N should cross at T_c if it is a second-order transition. Note, however, that when a marginal phase exists, these curves should collapse rather than cross for all the critical region [33].

The plots of B_m versus T are shown in Fig. 5(a) for different values of N at $\sigma = 0.3$. It is apparent that all curves intersect at a precise temperature, allowing us to extract the Curie temperature $T_c(\sigma)$, and permitting us to establish a clear-cut boundary between the PM and FM phases. The relatively modest system sizes that we have used (a limitation due to the long-range nature of the dipolar interaction) does not allow a precise determination of the critical exponents.

However, from finite-size scaling relevant for dipolar Ising models, we get acceptable data-collapse plots of B_m versus $L^{3/2} \ln^{1/6} L\,(T/T_c - 1) + v\,(\ln L)^{-1/2}$ that provide a more reliable determination of T_c (see Fig. 6). This finite-size scaling behavior corresponds to the mean-field one and agrees with the fact that the upper critical dimension of the dipolar Ising

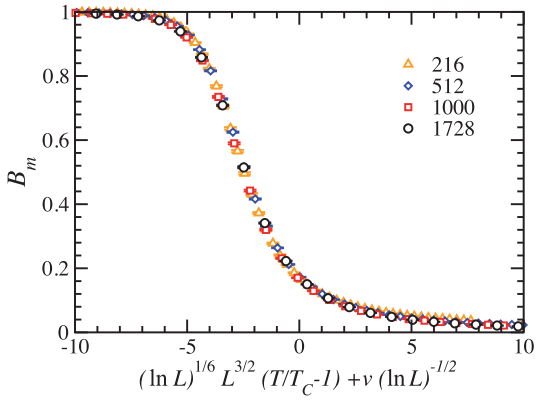

FIG. 6. Finite-size scaling plots for B_m vs $L^{3/2} (\ln L)^{1/6} (T/T_c - 1) + v (\ln L)^{-1/2}$ for $\sigma = 0.3$ using $T_C = 2.57(2)$ and $v = -1.83(8)$. $\triangle$, $\diamond$, $\square$, and $\circ$ stand for systems with $N = 216$, 512, 1000, and 1728, respectively.

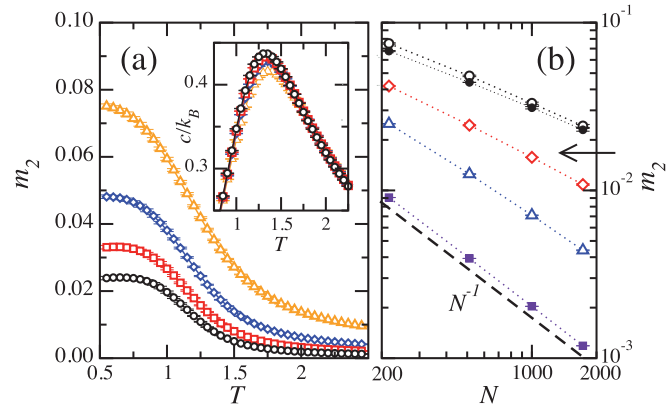

FIG. 7. (a) Plots of the squared magnetization m_2 vs T for $\sigma = 0.6$. Inset: the specific heat vs T. $\triangle$, $\diamond$, $\square$, and $\circ$ stand for $N = 216$, 512, 1000, and 1728 dipoles, respectively. All lines in this panel are guides to the eye. (b) Log-log plots of m_2 vs N for $\sigma = 0.6$. From top to bottom: $\circ$, $\bullet$, $\diamond$, $\triangle$, and $\blacksquare$ stand for temperatures $T = 0.55$, 0.85, 1.25, 1.55, and 2.55, respectively. The arrow marks the onset of the PM phase. Dotted lines are guides to the eye. The dashed line shows the N^{-1} decay expected for a paramagnet in the thermodynamic limit.

model is $d_u = 3$ [34,35]. For $\sigma = 0.3$, we get $T_c = 2.57(2)$. Likewise, precise determinations of $T_c(\sigma)$ can be obtained for $\sigma \leqslant 0.53$, the overall result being shown in Fig. 2.

For $\sigma = 0.55$ and 0.57, the curves B_m versus T merge rather than cross at low temperatures, giving a less precise determination of T_c. We will return to this point in Sec. III C. Given that for our model $\vec{m}$ does not rotate, m_z and the overlap q are expected to give similar information in the FM phase. Thus, crossing points in the plots of B_q versus T, like the ones shown in Fig. 5(b), may in principle provide an additional way to obtain T_c. This is true for $\sigma \geqslant 0.53$ for which clean crossing points are obtained. For smaller values of σ, see Fig. 5(b), a characteristic dip near the transition temperature makes it difficult to accurately locate the critical point [36].

B. The SG phase

This subsection is devoted to the study of small texturations, which quantitatively entails large values of σ. As σ grows, we observe large sample-to-sample fluctuations, which obliges us to increase the number of samples up to roughly 10 000 (see Table I) in order to attain trustworthy averages. Also large relaxation times are observed, a typical feature of SG behavior. Indeed, we are going to report numerical data that evidence the absence of magnetic order and the existence of an equilibrium SG phase for systems with $\sigma \geqslant 0.6$. With the aim of exploring this low-temperature ordered phase within a reasonable amount of computer time, we have performed the TMC simulations at temperatures no less than $T = 0.55$ and system sizes no larger than $N = 1728$, to the detriment of the accuracy.

Plots of the moment m_2 versus T are shown in Fig. 7(a) at $\sigma = 0.6$. m_2 decreases as N increases at all temperatures. In the inset of the figure, we show the plots of the specific heat c/k_B versus T. They display a gentle variation, and no signature of any possible singularity is seen. Similar graphs follow if the study is repeated at larger values of σ. These are pieces of evidence that point to the nonexistence of FM order and of any PM-FM transition for $\sigma \geqslant 0.6$.

In Fig. 7(b) we show log-log plots of m_2 versus N. They exhibit a decay faster than $1/N^{1/2}$ for all available temperatures. At low temperatures $T \lesssim 1$ the results are in principle consistent with quasi-long-range magnetic order. We will further discuss this point in the next subsection. For the PM phase (with short-range magnetic order), we expect to observe $m_2 \sim 1/N$ for large enough systems. For the available system sizes, we discern such a trend only for extremely large temperatures (see, for example, the data at $T = 2.55$).

A definite signature of the presence of a SG phase is the divergence of the magnetic susceptibility at low temperatures. The plots of χ_m versus T for $\sigma = 0.6$ showing an increase with N, see Fig. 8(a), are consistent with that scenario. Notice that this is in clear contrast with the behavior shown in Fig. 4(b) for $\sigma = 0.3$. Log-log plots of χ_m versus N for low temperatures show a power-law increase $\chi_m \sim N^p$ with an

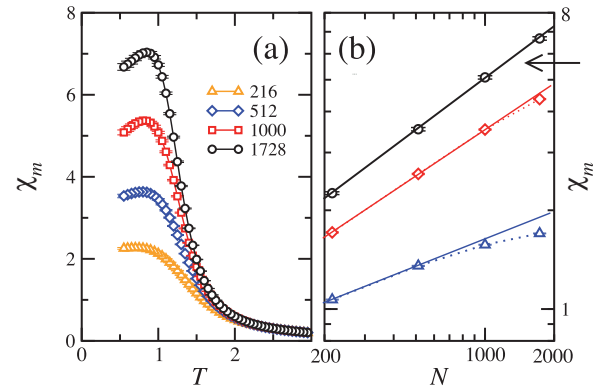

FIG. 8. (a) Plots of the magnetic susceptibility χ_m vs T for $\sigma = 0.6$. $\triangle$, $\diamond$, $\square$, and $\circ$ stand for systems with $N = 216$, 512, 1000, and 1728 dipoles, respectively. Solid lines are guides to the eye. (b) Log-log plots of χ_m vs N for $\sigma = 0.6$. $\circ$, $\diamond$, and $\triangle$ stand for temperatures $T = 0.55$, 1.25, and 1.55, respectively. As stressed by the dotted lines connecting the points, data cease to grow linearly (the solid lines) at large temperatures. The arrow marks the onset of the PM phase.

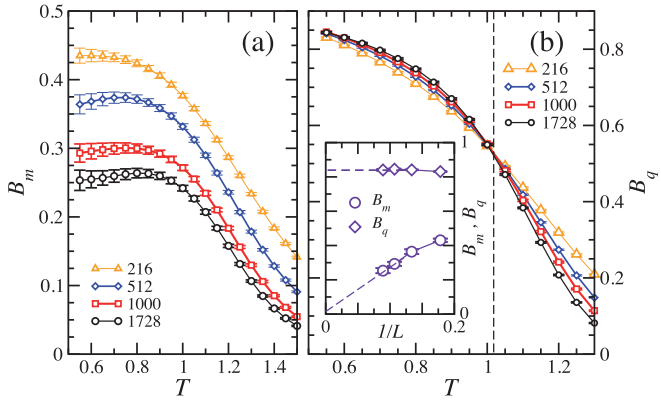

FIG. 9. (a) Plots of B_m vs T for $\sigma = 0.6$. △, ◇, □, and ○ denote $N = 216$, 512, 1000, and 1728 dipoles, respectively. The solid lines are guides to the eye. (b) Plots of B_q vs T. Same symbols as in (a). The curves cross at the SG transition temperature, marked in the figure with a vertical dashed line. The inset contains plots of B_m and B_q vs $1/L$ for the lowest temperature available, $T = 0.55$. ○ (◇) stands for B_m (B_q). The dashed lines in the inset are extrapolations.

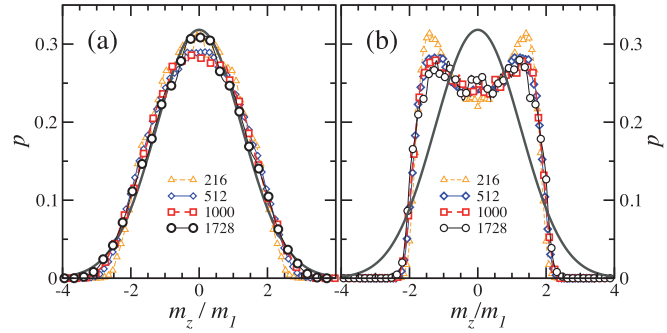

FIG. 10. (a) Plots of the probability distribution $p(m_z/m_1)$ for $\sigma = 0.6$ and $T = 0.55$. △, ◇, □, and ○ stand for $N = 216$, 512, 1000, and 1728, respectively. The thick solid line is the typical Gaussian distribution for paramagnets in the $N \to \infty$ limit. (b) Same as in (a) but for $\sigma = 0.55$. The thin lines connecting data in both panels are guides to the eye.

exponent p that changes slightly with T but that is never greater than $p = 0.55$ [see Fig. 8(b)]. For $T \gtrsim 1.25$, the curves detach from an algebraic growth and bend downward indicating a nondiverging χ_m in the macroscopic limit, as expected for a PM phase.

The most convincing evidence for the absence of FM order at low temperatures for $\sigma = 0.6$ is given in Fig. 9(a). The B_m versus T plots show that B_m diminishes as N increases for all temperatures. As a consequence, curves for different system sizes do not cross, in contrast with the behavior found in Fig. 5(a). Recall that, in the case of short-range FM order, B_m should vanish in the thermodynamic limit. In the inset of Fig. 9(b), we have represented B_m versus $1/L$ for $T = 0.55$, showing that that is indeed the case. We obtain a similar trend for all $\sigma \geqslant 0.6$ and temperatures. This finding, consistent with short-range FM order, seems to be in contradiction with the effective power-law decay of m_2 with N observed for low T for the system sizes we have used [see Fig. 7(b)]. Some clues could be obtained by inspecting the two independent magnetic configurations displayed in Fig. 1. These are thermalized configurations at $\sigma = 0.6$, $T = 0.55$ in the largest system size considered in this work, $N = 1728$. The sample appears to be broken into large magnetic domains whose frontiers appear to be frozen. The large size of the domains explains the effective power-law decay found in the m_2 versus N plots in Fig. 7(b). In striking contrast, the overlap between the two configurations covers practically the whole system [see Fig. 1(c)], suggesting a diverging SG overlap correlation length.

Provided that the magnetic correlation length (i.e., the size of the magnetic domains) does not diverge, then m_z would be expected to be normally distributed, as follows from the law of large numbers. In Fig. 10(a) we represent the distribution $p(m_r)$ where $m_r \equiv m_z/m_1$ averaged over all samples for $\sigma = 0.6$ and the lowest temperature available, $T = 0.55$. Clearly, $p(m_r)$ tends to $(1/\pi)\exp(-m_r^2/\pi)$ as $N \to \infty$, in agreement with short-range magnetic order. We obtain qualitatively similar results for all $\sigma \geqslant 0.6$ and T, a fact that leads us to discard the existence of a critical FM phase with quasi-long-range order at low temperature. For this to be the case, we should have seen a non-Gaussian broad distribution $p(m_r)$ that behaves as a scaling function that does not change with the system size [37]. It seems to be the case, within errors, for a bit larger texturation ($\sigma = 0.55$), as shown in Fig. 10(b) for $T = 0.55$. More details on this point will be discussed in the next subsection.

Finally, we report numerical evidence in favor of the positive existence of a SG phase for $\sigma \gtrsim 0.6$ by studying the overlap parameter q_2 and B_q. Plots of q_2 versus T are shown in Fig. 11(a) for $\sigma = 0.6$. It is worth comparing this figure with its counterpart for m_2, Fig. 7(a), to appreciate the qualitative differences between the behavior of q_2 and m_2 at low temperature. Note, however, that q_2 also decreases

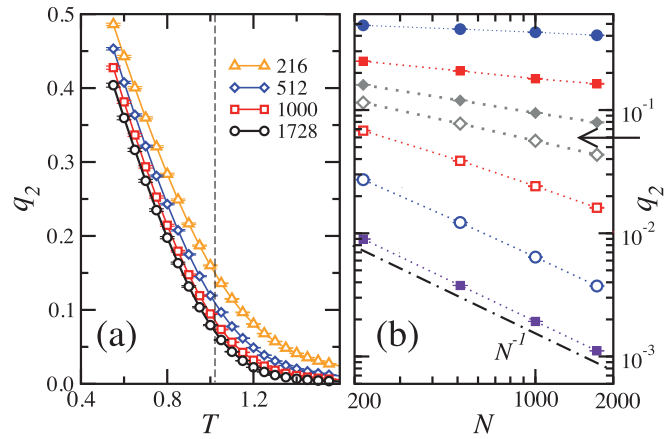

FIG. 11. (a) Plots of the squared overlap parameter q_2 vs T for $\sigma = 0.6$. △, ◇, □, and ○ stand for $N = 216$, 512, 1000, and 1728, respectively. The dashed vertical line indicates the SG transition temperature. Solid lines are guides to the eye. (b) Log-log plots of q_2 vs the number of dipoles N for $\sigma = 0.6$. From top to bottom: •, ■, ♦, ◇, □, ○, and △ stand for $T = 0.55$, 0.85, 1.0, 1.05, 1.25, 1.55, and 2.55, respectively. The arrow marks the onset of the PM phase. Dotted lines are guides to the eye. The dot-dashed line shows the N^{-1} decay expected for the PM phase.

appreciably as N increases for all temperatures. This fact raises the question on whether or not q_2 vanishes as $L \to \infty$. To clarify this, we have prepared the log-log plots of q_2 versus N shown in Fig. 11(b). Data are consistent with $q_2 \sim 1/N^p$ for low temperatures, and with a T-dependent exponent p. The N^{-1} trend, expected for PM phases, shows up only at large temperatures. All of this suggests the presence of a phase with quasi-long-range SG order. We draw additional evidence on this point from the behavior of B_q. Recall that in the thermodynamic limit, $B_q \to 1$ in the case of strong long-range order, it vanishes in the PM phase, and it tends to some intermediate value at criticality. In Fig. 9(b), plots of B_q versus T for $\sigma = 0.6$ show that curves of different system sizes cross at a precise temperature T_{sg} that delimits the extent of the region with SG order. These crossings permit us to obtain the points $T_{sg}(\sigma)$ of the PM-SG transition line in Fig. 2 [38]. Note that T_{sg} does not vary strongly with σ. The results agree well with the limiting value $T_{sg} = 0.8$ found in previous work for the RAD case ($\sigma = \infty$) [17]. It is important to stress that the fact that the B_q curves cross at T_{sg} does not imply the existence of strong long-range order for $T < T_{sg}$ [39]. Indeed, plots of B_q versus $1/L$ for $T \leqslant T_{sg}(\sigma)$ show that B_q stays below 1 [see the inset in Fig. 9(b)]. Then, the B_q curves should collapse in the $N \to \infty$ limit when $T \leqslant T_{sg}(\sigma)$, which is consistent with the algebraic decay found for q_2.

In summary, the data for $\sigma \geqslant 0.6$ point to the existence of a SG phase delimited by $T_{sg}(\sigma)$ for which quasi-long-range SG order occurs, like in the 2D XY model [40,41]. A similar SG phase has been previously found for other dipolar systems with strong frozen disorder, namely for systems of parallel Ising dipoles with strong dilution [30,39] as well as in dense arrays, both crystalline and noncrystalline, of nontextured systems of Ising dipoles with the axes oriented completely at random [17,42]. However, given the moderate range of system sizes considered here, our data cannot rule out completely the so-called replica symmetry-breaking scenario in which q_2 does not vanish in the $N \to \infty$ limit, but there are long-range SG order fluctuations that provoke $B_q < 1$ [43,44].

C. The FM-SG transition

From the previous sections, we expect to find a transition within the narrow region $0.53 < \sigma < 0.6$. To identify it, we have carried out TMC simulations for several values of σ in the interval $[0.45, 0.6]$ and a range of temperatures in the TMC between $T_{max} = 3.5$ and $T_{min} = 0.55$. The highest temperature has been chosen well into the PM phase in order to refresh configurations and ensure equilibrium results for $T_{min} = 0.55$, which is, in turn, a temperature very deep in the low-temperature phase. This procedure facilitates the exploration of the FM boundary along several isothermal lines, allowing us to investigate whether there is an intermediate phase between this boundary and the SG phase determined in the previous section. In addition, the slope of the FM boundary line may discern between a forward or a reentrant behavior.

The magnetization m_2 versus σ in Fig. 12(a) for a low temperature, $T = 0.55$, shows that m_2 decreases with N for $\sigma > 0.5$. Log-log plots of m_2 versus N in Fig. 12(b) show that the m_2 curves deviate from an algebraic decay to bend upward at $\sigma = 0.53$, indicating also a nonvanishing magnetization. In

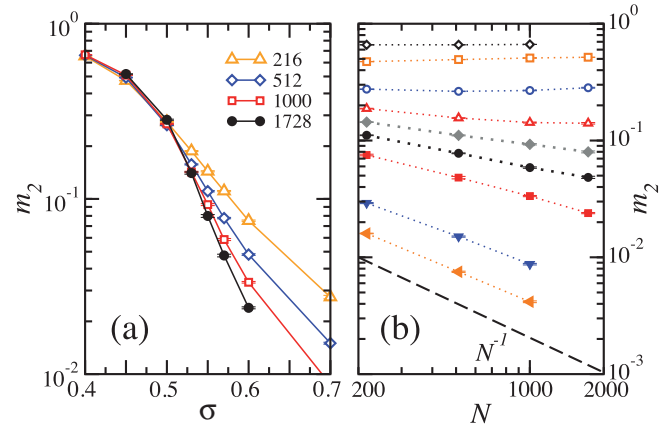

FIG. 12. (a) Semilog plots of the squared magnetization m_2 vs σ for the lowest available temperature, $T = 0.55$. △, ◇, □, and ○ stand for $N = 216$, 512, 1000, and 1728, respectively. Solid lines are guides to the eye. (b) Log-log plots of m_2 vs the number of dipoles N at $T = 0.55$. From top to bottom: ◇, □, ○, △, ♦, ●, ■, ▼, and ◄ stand for $\sigma = 0.4$, 0.45, 0.5, 0.53, 0.55, 0.57, 0.6, 0.7, and 0.8, respectively. Dotted lines are guides to the eye. The dashed line shows the N^{-1} decay expected for the paramagnetic phase.

contrast, for $\sigma = 0.55$ and 0.57 we find a power-law decay, giving some room for the existence of an intermediate region with quasi-long-range FM order. This decay is consistent with the behavior found for the $p(m_r)$ distributions of Fig. 10(b) for $\sigma = 0.55$. All $p(m_r)$ curves tend to collapse into a non-Gaussian broad distribution for large N, as expected when quasi-long-range order settles. We obtain the same qualitative results for $\sigma = 0.57$. Finally, curves for larger values of σ tend to the N^{-1} decay characteristic of short-range FM order, as discussed in the previous section.

The plots for q_2 are shown Fig. 13. Similarly as for m_2, q_2 does not vanish for $\sigma \leqslant 0.53$, as is expected for a FM phase.

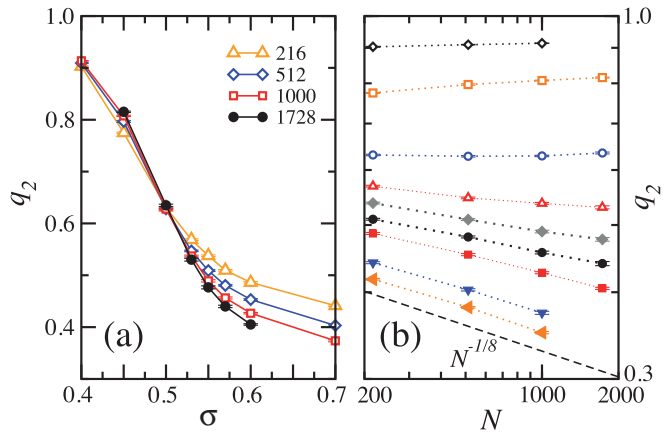

FIG. 13. (a) Plots of the squared overlap parameter q_2 vs σ for the lowest available temperature, $T = 0.55$. △, ◇, □, and ○ stand for $N = 216$, 512, 1000, and 1728, respectively. Solid lines are guides to the eye. (b) Log-log plots of q_2 vs the number of dipoles N for $T = 0.55$. From top to bottom: ◇, □, ○, △, ♦, ●, ■, ▼, and ◄ stand for $\sigma = 0.4$, 0.45, 0.5, 0.53, 0.55, 0.57, 0.6, 0.7, and ∞, respectively. Dotted lines are guides to the eye. The dashed line corresponds approximately to an $N^{-1/8}$ decay.

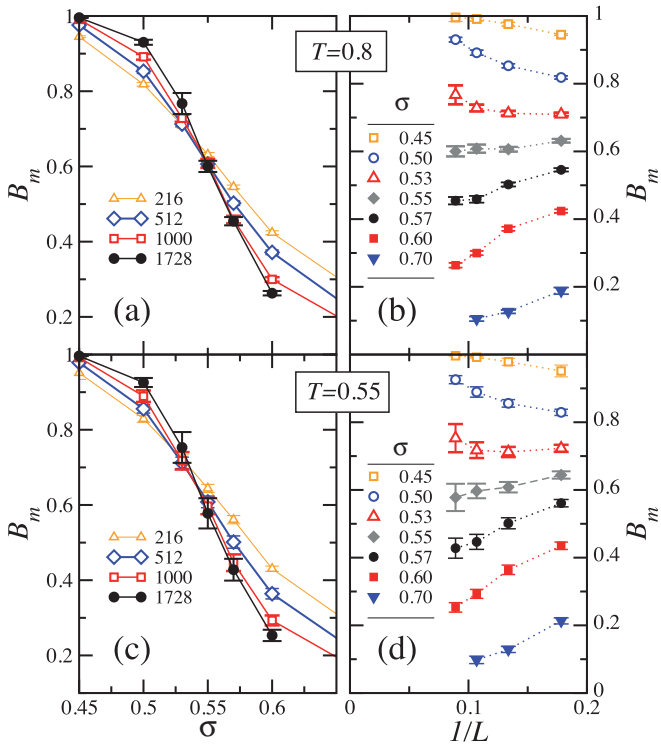

FIG. 14. (a) Plots of B_m vs σ for $T = 0.8$, and the values of N indicated in the panel. Solid lines are guides to the eye. (b) Plots of B_m vs $1/L$ for $T = 1$ for various values of σ. From top to bottom: □, ○, △, ♦, ●, ■, and ▼ stand for $\sigma = 0.45$, 0.5, 0.53, 0.55, 0.57, 0.6, and 0.7, respectively. Dotted lines are guides to the eye. (c) Same as in (a) but for $T = 0.55$. (d) Same as in (b) but for $T = 0.55$.

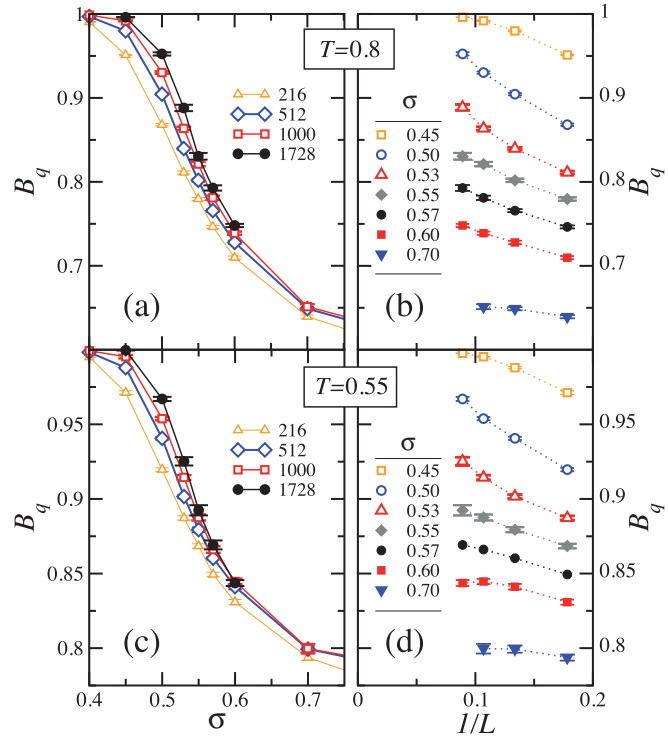

FIG. 15. (a) Plots of B_q vs σ for $T = 0.8$, and the values of N indicated in the panel. Solid lines are guides to the eye. (b) Plots of B_m vs $1/L$ for $T = 1$ for various values of σ. From top to bottom: □, ○, △, ♦, ●, ■, and ▼ stand for $\sigma = 0.45$, 0.5, 0.53, 0.55, 0.57, 0.6, and 0.7, respectively. Dotted lines are guides to the eye. (c) Same as in (a) but for $T = 0.55$. (d) Same as in (b) but for $T = 0.55$.

For larger values of σ we find instead a $1/N^p$ algebraic decay of q_2. Note that the slope of the decay is small. For example, for $\sigma \geqslant 0.7$ we find $p \approx 1/8$, indicating that we are far from a PM phase (for which $p = 1$ is expected).

We next examine how the cumulants B_m and B_q vary with σ and N at low temperatures. For the FM phase both quantities tend to 1 in the thermodynamic limit, while for the SG phase B_m should vanish as $N \to \infty$, and B_q should tend to a nonzero value. Then, if there is a transition line separating the FM and the SG phases, we expect the related B_m versus σ curves to cross at the transition point $\sigma_c(T)$. As for the B_q versus σ curve, it should merge for $\sigma \geqslant \sigma_c$ and splay out only for $\sigma < \sigma_c$.

In Fig. 14(a) we show plots of B_m versus σ for $T = 0.8$, a temperature that lies below the PM boundary. Curves for different sizes do not cross at a precise point but rather tend to collapse in the intermediate region $0.55 \lesssim \sigma \lesssim 0.57$ as N increases. They only splay out for $\sigma \lesssim 0.53$ and for $\sigma \gtrsim 0.6$. Plotting instead B_m versus $1/L$ for several values of σ, as shown in Fig. 14(b), we see that B_m tends to values that are neither 1 nor 0, which is a trait of quasi-long-range order, only in this intermediate region. Similar plots are given for a lower temperature, $T = 0.55$, in panels (c) and (d) of the same figure. We obtain the same qualitative picture found for $T = 0.8$, apart from the fact that finite-size effects are larger within the intermediate region. However, $1/L$ extrapolations of B_m for $\sigma = 0.55$ and 0.57 tend to nonvanishing values, which is consistent with marginal behavior. We have performed averages over thousands of samples in order to improve the statistics. However, the error bars of B_m do not allow a precise determination of the FM boundary $\sigma_c(T)$. The points along the FM boundary shown in Fig. 2 are just rough estimates obtained by taking the mean value of the crossing points of the pairs of curves B_m versus σ for different sizes $(N_1, N_2) = (8^3, 10^3)$ and $(10^3, 12^3)$. We find a boundary line that is nearly vertical with a positive slope suggesting a slight reentrance near $\sigma = 0.55$. However, at least for the system sizes we have employed, plots of m_2 versus T for $\sigma = 0.55$ do not allow us to discern any intermediate region with strong FM order separating the low-temperature SG phase from the PM region (not shown). More extensive simulations for larger systems and for additional values of σ within the interval (0.53,0.6) would be needed to address this issue. In summary, the results point to the existence of a narrow intermediate region with quasi-long-range order between the FM boundary line and the SG phase, a phase that covers the low-temperature region for all $\sigma \geqslant 0.6$. For $\sigma = 0.57$ and all temperatures below the PM boundary, we obtain a nonvanishing B_m and an algebraic decay of m_2 with N, indicating that that region of the T-σ plane still stays in the quasi-long-range regime. The area shaded gray in Fig. 2 exhibits the extent of this intermediate phase.

Additional information could be gathered from a comparison of the plots in Fig. 14 with their counterparts for B_q versus σ shown in Fig. 15. Note that, in contrast to B_m, the

curves of B_q versus σ do not splay out for $\sigma \geqslant 0.6$ but merge for large N. This is expected for the SG phase described in the previous section. On the other hand, for $\sigma \leqslant 0.53$ we find that both B_m and B_q tend to 1 in the thermodynamic limit, indicating the existence of strong FM order. Finally, for $\sigma = 0.55$ and 0.57 (the only values we have simulated in the intermediate region), B_q increases with the size of the system. $1/L$ extrapolations of B_q for $T = 0.55$ point to values that are less than 1, suggesting that the intermediate phase includes quasi-long-range FM and SG order contemporaneously. Note, however, that the data for $T = 0.8$ shown in Fig. 15(b) do not exclude the possibility of having strong SG order in this intermediate region. Simulations for larger systems far beyond our present CPU-time resources would be needed in order to address this point.

IV. CONCLUSIONS

We have studied by Monte Carlo simulations the effect of texturation on the collective behavior of disordered dense packings of identical magnetic nanospheres that behave like Ising dipoles along local easy axes. The local axes orientations follow a probability distribution parametrized by a single parameter σ. This allows us to vary the amount of orientational disorder ranging from the complete textured case ($\sigma = 0$) with all axes pointing along a common direction, to the nontextured one with the axes oriented at random ($\sigma = \infty$).

We have obtained the phase diagram on the temperature-σ plane (see Fig. 2) from studying the magnetization, the spin-glass overlap parameter q, their fluctuations, as well as some other related observables; see Sec. II D. The region $\sigma \leqslant 0.53$ contains a low-temperature ferromagnetic phase with strong order separated by a second-order transition line from a paramagnetic high-temperature phase. For large orientational disorder (namely, for $\sigma \geqslant 0.6$) the ferromagnetic order gives way to a spin-glass phase for temperatures below a nearly flat transition line $T_{sg}(\sigma)$ that extends up to $T_{sg}(\infty) = 0.8$. The spin-glass phase is similar to the one previously observed in systems of Ising dipoles with strong structural disorder, at $\sigma = \infty$. The Binder cumulants allow us to estimate the position of the low-temperature boundary separating the ferromagnetic and spin-glass phases. It is located near $\sigma = 0.55$ and consistent with a small reentrance. Moreover, a narrow intermediate region with quasi-long-range ferromagnetic order seems to lie between the ferromagnetic and the spin-glass phases.

Finally, we comment on the applicability of our results to actual experimental situations. As stated in the Introduction, the model corresponds to the limit $T_c/T_b \gg 1$, where T_b is the blocking temperature of the dispersed system and T_c is a dipolar ordering temperature. This is, for instance, the situation of the maghemite NP ensembles with diameters d of 6 nm $< d <$ 12 nm studied in Ref. [7]. In them, PM/SG freezing is observed for randomly distributed easy axes and a volume fraction $\phi \sim 0.67$ at a ratio of temperatures $4 < T_c/T_b < 12$. Moreover, the aging phenomenon used to characterize the SG state is observable only at temperatures above T_b. We can thus conclude that the present model applies at a qualitative level to the latter experimental situations whenever the SG region of the phase diagram is reached.

ACKNOWLEDGMENTS

We thank the Centro de Supercomputación y Bioinformática at University of Málaga, Institute Carlos I at University of Granada, and Cineca for their generous allocations of computer time in clusters Picasso and Proteus. We gratefully acknowledge access to the HPC resources of CINES under the Allocation No. 2018-A0040906180 made by GENCI, CINES, France. Work performed under Grants No. FIS2017-84256-P (FEDER funds) from the Spanish Ministry and the Agencia Española de Investigación (AEI), SOMM17/6105/UGR from Consejería de Conocimiento, Investigación y Universidad, Junta de Andalucía and European Regional Development Fund (ERDF), and No. ANR-CE08-007 from the ANR French Agency. J.J.A. also thanks the Italian "Fondo FAI" for financial support. Each author also gratefully acknowledges the warm hospitality received during their stays in the other authors' institutes: ICMPE, the Pisa INFN section, and the University of Málaga.

[1] R. F. Wang, C. Nisoli, R. S. Freitas, J. Li, W. McConville, B. J. Cooley, M. S. Lund, N. Samarth, C. Leighton, V. H. Crespi, and P. Schiffer, Nature (London) **439**, 303 (2006).

[2] S. Bedanta and W. Kleeman, J. Phys. D **42**, 013001 (2009); S. A. Majetich and M. Sachan, *ibid.* **39**, R407 (2006).

[3] R. P. Cowburn, Philos. Trans. R. Soc. London A **358**, 281 (2000); R. J. Hicken, *ibid.* **361**, 2827 (2003).

[4] D. Fiorani and D. Peddis, J. Phys. Conf. Ser. **521**, 012006 (2014).

[5] S. Nakamae, J. Magn. Magn. Mater. **355**, 225 (2014).

[6] R. Skomski, J. Phys.: Condens. Matter **15**, R841 (2003).

[7] J. A. De Toro, S. S. Lee, D. Salazar, J. L. Cheong, P. S. Normile, P. Muñiz, J. M. Riveiro, M. Hillenkamp, F. Tournus, A. Amion, and P. Nordblad, Appl. Phys. Lett. **102**, 183104 (2013); M. S. Andersson, R. Mathieu, S. S. Lee, P. S. Normile, G. Singh, P. Nordblad, and J. A. De Toro, Nanotechnology **26**, 475703 (2015).

[8] P. Allia, M. Coisson, P. Tiberto, F. Vinai, M. Knobel, M. A. Novak, and W. C. Nunes, Phys. Rev. B **64**, 144420 (2001).

[9] E. Josten, E. Wetterskog, E. Glavic, P. Boesecke, A. Feoktystov, E. Brauweiler-Reuters, U. Rücker, G. Salazar-Alvarez, T. Brückel, and L. Bergström, Sci. Rep. **7**, 2802 (2017).

[10] A. T. Ngo, S. Costanzo, P. Albouy, V. Russier, S. Nakamae, J. Richardi, and I. Lisiecki, Colloids Surf. A **560**, 270 (2019).

[11] J. Luttinger and L. Tisza, Phys. Rev. **70**, 954 (1942); J. F. Fernández and J. J. Alonso, Phys. Rev. B **62**, 53 (2000).

[12] S. Sahoo, O. Petracic, W. Kleemann, P. Nordblad, S. Cardoso, and P. P. Freitas, Phys. Rev. B **67**, 214422 (2003).

[13] S. Nakamae, C. Crauste-Thibierge, D. L'Hôte, E. Vincent, E. Dubois, V. Dupuis, and R. Perzynski, Appl. Phys. Lett. **101**, 242409 (2010).
[14] S. Mørup, Europhys. Lett. **28**, 671 (1994).
[15] V. Russier, C. de Montferrand, Y. Lalatonne, and L. Motte, J. Appl. Phys. **114**, 143904 (2013); V. Russier, J. Magn. Magn. Mater. **409**, 50 (2016); M. Woińska, J. Szczytko, A. Majhofer, J. Gosk, K. Dziatkowski, and A. Twardowski, Phys. Rev. B **88**, 144421 (2013).
[16] S. Torquato and F. H. Stillinger, Rev. Mod. Phys. **82**, 2633 (2010).
[17] J. J. Alonso and B. Alles, J. Phys.: Condens. Matter **29**, 355802 (2017).
[18] G. Ayton, M. J. P. Gingras, and G. N. Patey, Phys. Rev. Lett. **75**, 2360 (1995).
[19] G. Ayton, M. J. P. Gingras, and G. N. Patey, Phys. Rev. E **56**, 562 (1997).
[20] S. Nakamae, C. Crauste-Thibierge, K. Komatsu, D. L'Hôte, E. Vincent, E. Dubois, V. Dupuis, and R. Perzynski, J. Phys. D **43**, 474001 (2010).
[21] J. J. Weis and D. Levesque, Phys. Rev. E **48**, 3728 (1993)
[22] J. J. Weis, J. Chem. Phys. **123**, 044503 (2005).
[23] B. D. Lubachevsky and F. H. Stillinger, J. Stat. Phys. **60**, 561 (1990).
[24] M. Skoge, A. Donev, F. H. Stillinger, and S. Torquato, Phys. Rev. E **74**, 041127 (2006).
[25] E. Marinari and G. Parisi, Europhys. Lett. **19**, 451 (1992); K. Hukushima and K. Nemoto, J. Phys. Soc. Jpn. **65**, 1604 (1996).
[26] N. A. Metropolis, A. W. Rosenbluth, M. N. Rosenbluth, A. H. Teller, and E. Teller, J. Chem. Phys. **21**, 1087 (1953).
[27] P. Ewald, Ann. Phys. (Leipzig) **369**, 253 (1921).
[28] Z. Wang and C. Holm, J. Chem. Phys. **115**, 6351 (2001).
[29] M. P. Allen and D. J. Tildesley, *Computer Simulation of Liquids*, 1st ed. (Clarendon, Oxford, 1987).
[30] J. J. Alonso, Phys. Rev. B **91**, 094406 (2015).
[31] T. Aspelmeier, A. Billoire, E. Marinari, and M. A. Moore, J. Phys. A **41**, 324008 (2008).
[32] S. F. Edwards and P. W. Anderson, J. Phys. F **5**, 965 (1975).
[33] H. G. Ballesteros, A. Cruz, L. A. Fernandez, V. Martín-Mayor, J. Pech, J. J. Ruiz-Lorenzo, A. Tarancón, P. Téllez, C. L. Ullod, and C. Ungil, Phys. Rev. B **62**, 14237 (2000).
[34] A. Aharony, Phys. Rev. B **8**, 3363 (1973).
[35] A. V. Klopper, U. K. Rossler, and R. L. Stamps, Eur. Phys. J. B **50**, 45 (2006).
[36] H. Hong, H. Park, and L. Tang, J. Korean Phys. Soc. **49**, L1885 (2006).
[37] At criticality, the probability distribution of m_z behaves as $P(m_z) = L^{(1+\eta)/2} p(m_z L^{(1+\eta)/2})$, where p is a scale-invariant function, and $m_1 \sim L^{-(1+\eta)/2}$.
[38] For some values of σ, pairs of curves do not cross precisely at the same point, but $1/L$ extrapolations of the crossing points allow us to obtain proper values of $T_{\rm sg}$.
[39] J. J. Alonso and J. F. Fernández, Phys. Rev. B **81**, 064408 (2010).
[40] J. M. Kosterlitz and D. J. Thouless, J. Phys. C **6**, 1181 (1973); J. M. Kosterlitz, *ibid.* **7**, 1046 (1974).
[41] J. F. Fernández, M. F. Ferreira, and J. Stankiewicz, Phys. Rev. B **34**, 292 (1986); H. G. Evertz and D. P. Landau, *ibid.* **54**, 12302 (1996).
[42] J. F. Fernández, Phys. Rev. B **78**, 064404 (2008); J. F. Fernández and J. J. Alonso, *ibid.* **79**, 214424 (2009).
[43] G. Parisi, Phys. Rev. Lett. **43**, 1754 (1979); **50**, 1946 (1983).
[44] D. L. Stein and C. M. Newman, *Spin Glasses and Complexity* (Princeton University Press, Princeton, NJ, 2012).